JMEPEG (2024) 33:7659–7669
https://doi.org/10.1007/s11665-024-09460-0

©The Author(s)
1059-9495/$19.00

ORIGINAL RESEARCH ARTICLE

In Situ Analysis of Stress and Microstructure Evolution during Welding of High-Alloy Steels Using Energy-Dispersive X-Ray Diffraction

Nico Hempel, Thomas Nitschke-Pagel, Manuela Klaus, Daniel Apel, Christoph Genzel, and Klaus Dilger

Submitted: 16 June 2023 / Revised: 26 November 2023 / Accepted: 8 March 2024 / Published online: 22 April 2024

Constrained thermal expansion and contraction during welding cause a compression-tension cycle and plastic deformation in the heat-affected zone, leading to work hardening. The nature of this hardening effect—isotropic or kinematic—determines the final local yield stress and thus affects the residual stress state. Therefore, mechanical hardening must be modeled correctly in welding simulations for accurately predicting welding residual stresses. Previous studies, relying on comparisons with experimental ex situ results, led to different recommendations regarding the choice of the hardening model and thus require clarification. In this work, the stress evolution in the heat-affected zone of a tungsten inert gas weld is studied in situ using energy-dispersive x-ray diffraction and a novel method of stress analysis based on crystallite anisotropy. Additionally, microstructural information is gathered through line profile analysis. Results are shown for both austenitic and ferritic high-alloy steels and compared to ex-situ results including a validation of the new method of stress analysis. Finally, conclusions on the nature of work hardening are drawn.

Keywords austenitic steel, diffraction elastic constants, ferritic steel, in-situ analysis, residual stress, welding, X-ray diffraction

1. Introduction

Fusion welding is characterized by a temperature field that is inhomogeneous in both space and time. The highly heated material expands, but is mechanically constrained by surrounding cooler material, which causes compressive stress and plastic deformation in the former. Due to the resulting incompatibilities, thermal shrinkage during cooling then leads to tensile stresses and again plastic deformation. In the heat-affected zone (HAZ), where temperatures are high but below the solidus temperature, the thermal cycle therefore causes cyclic plastic deformation, see, e.g. (Ref 1) for a more detailed description.

In numerical welding simulations used for computing residual stresses and distortion, the material model must contain assumptions on the nature of work hardening resulting from the cyclic plastic deformation. For isotropic hardening, the hardening effect obtained in an arbitrary load direction is valid for all directions, whereas kinematic hardening leads to hardening in the load direction, but to softening in the opposite direction, most notably observed in the well-known Bauschinger effect, see, e.g. (Ref 2). Also, mixed models that combine both characteristics are known, such as (Ref 3). Due to the cyclic plastic deformation during welding, using a realistic material model is important for correctly computing the local yield stress and thereby the residual stress state.

Several authors have investigated the question which hardening model should be used in welding simulations by comparing the results of numerical simulations to experimentally analyses residual stresses. In a round robin organized by the International Institute of Welding, a two-pass weld on an austenitic steel plate was analyzed and it was found that the purely isotropic model agreed best with experimental results (Ref 4, 5). Several notable activities were conducted by the Network on Neutron Techniques Standardization for Structural Integrity (NeT), e.g., investigating an austenitic one-pass or three-pass weld, see the summaries by Smith et al. in (Ref 6, 7), respectively. Here, a mixed model containing both isotropic and kinematic characteristics was recommended. The same result was obtained by Deng et al. (Ref 8) for austenitic steel and by Ottersböck et al. (Ref 9) and Häberle et al. (Ref 10) for structural steel. However, previous own work that considered not only the residual stress state, but also the hardening in terms

This invited article is part of a special topical issue of the *Journal of Materials Engineering and Performance* on Residual Stress Analysis: Measurement, Effects, and Control. The issue was organized by Rajan Bhambroo, Tenneco, Inc.; Lesley Frame, University of Connecticut; Andrew Payzant, Oak Ridge National Laboratory; and James Pineault, Proto Manufacturing on behalf of the ASM Residual Stress Technical Committee.

Nico Hempel, TUM School of Engineering and Design, Department of Materials Engineering, Chair of Materials Engineering of Additive Manufacturing, Technical University of Munich, Freisinger Landstr. 52, 85748 Garching, Germany; and TU Braunschweig, Institute of Joining and Welding, Langer Kamp 8, 38106 Braunschweig, Germany; **Thomas Nitschke-Pagel** and **Klaus Dilger**, TU Braunschweig, Institute of Joining and Welding, Langer Kamp 8, 38106 Braunschweig, Germany; and **Manuela Klaus, Daniel Apel,** and **Christoph Genzel**, Helmholtz-Zentrum Berlin für Materialien und Energie, Hahn-Meitner-Platz 1, D-14109 Berlin, Germany. Contact e-mail: nico.hempel@tum.de.

of the microstrain, revealed a mainly isotropic character of the hardening in austenitic steel (Ref 11).

The disparity of the existing studies, which all relied on experimental data that was acquired ex situ, i.e., after welding, shows that further research is necessary for clarification. The main aim of this work is to study the evolutions of stress and work hardening *in situ* during welding at a synchrotron.

To this end, energy-dispersive x-ray diffraction (EDXRD) will be used. One of the main applications of EDXRD is the analysis of near-surface stress gradients due to the energy dependence of the penetration depth of the x-rays (Ref 12). However, EDXRD has also been used for in situ investigations, e.g., of the phase evolution during welding (Ref 13), or for quantitative analyses of the dislocation density (Ref 14). In this work, the stress evolution will be studied using a recently published method (Ref 15), which exploits the elastic anisotropy of the crystallites. Through the computation of relative strains between differently oriented grains and the differences in the diffraction elastic constant $\Delta(2S_1^{hkl})$, the average in-plane stress $\sigma_{||}$ can be computed without exact knowledge of the stress-free lattice parameter a_0. Since this so-called *transverse contraction method* is applied for the first time in this work, this paper is dedicated both to a practical validation of the method by comparing the results to those obtained by the conventional $\sin^2\psi$ method, and to analyzing the effects of the welding process on the evolutions of stress and work hardening.

2. Experimental Work

2.1 Materials and Sample Preparation

Samples were made of the metastable austenitic steel X2CrNi18-9 (1.4307/AISI 304L) and the ferritic steel X6Cr17 (1.4016/AISI 430), see the chemical compositions in Tables 1 and 2.

Both steels arrived in sheets of 10 mm thickness in hot-rolled condition. From these, plates of dimensions 200 × 150 × 10 mm^3 were cut. In order to reduce near-surface hardening effects and residual stress from the sheet production, the samples were heat-treated at 1050 °C for 12 min (X2CrNi18-9) or at 800 °C for 20 min (X6Cr17). During heat treatment, the samples were wrapped in anti-oxidation foil and the furnace was flushed with Argon. Afterward, the samples were cooled in forced air. The heat treatment caused a slight reduction in strength, see Tables 3 and 4. Moreover, anisotropic mechanical properties were observed in X6Cr17, see Table 4.

2.2 Welding

Mechanized tungsten inert gas (TIG) welding without filler metal was used for bead-on-plate welding, i.e., locally melting the plate material. The welding current and voltage were 200 A and 13,7 V, respectively, and the welding speed was 20 cm/min, yielding a nominal heat input of 8.2 kJ/cm. A mixture of each 50 % Argon and Helium was used as a shielding gas.

A 190 mm long weld bead was applied at the center of the plate, parallel to its long edge. During welding, the plate was seated loosely on three balls made of ZrO_2, one of which was placed below the zone of the in-situ measurements to keep it in place despite the distortion occurring during the welding process. Figure 1 shows the welding setup and the coordinate system.

In an identical ex-situ welding setup outside the synchrotron, temperature measurements with type K thermocouples were conducted at mid-length of the weld at different lateral distances. The data was synchronized with the synchrotron measurements.

2.3 Diffraction Measurements

All diffraction measurements were conducted at the former beamline station EDDI (Ref 16), optimized for energy-dispersive measurements, at the BESSY II electron storage ring operated by the Helmholtz-Zentrum Berlin für Materialien und Energie.

For the in-situ measurements, the welding setup described in 2.2 was tilted by 5° due to the invariably horizontal primary beam of the synchrotron, see Fig. 2. For each sample, one single area in the base material near the molten zone was observed throughout the welding process and subsequent cooling at mid-length of the weld (y = 100 mm) at a distance of x = 7 mm or x = 9 mm from the weld centerline, i.e., about 1.7 and 3.7 mm away from the weld toe, see also Fig. 1. The size of the gauge volume was defined by 2D double slits in both the primary and secondary beam path. The primary beam was confined to a cross-section of 1 × 1 mm^2, whereas the secondary beam was only limited in height to 0.1 mm. The bar-shaped gauge volume was completely immersed into the specimen. The diffraction angle was chosen to be $2\theta = 10.25°$, yielding a tilt angle $\psi \approx 0°$, i.e., the diffraction vector was nearly normal to the sample surface.

The diffraction spectrum of the originally "white" x-ray spectrum was recorded by an energy-dispersive detector in fixed position. The integration time of each diffractogram was 1 s for the first 300 s of a single experiment, including 57 s of welding and the first cooling stage. Afterward, diffractograms were integrated for 5 s within the next 300 s and for 10 s during the remainder of the experiment. Overall, every sample was observed for at least 1800 s. For a more reliable analysis of microstructure and stress, a moving integration was used, summing up the intensities of three consecutive diffractograms at any one time.

Additionally, diffraction measurements were conducted after welding, which is referred to as ex situ in the following. Here, several points at the sample surface along a line perpendicular to the welding direction, see Fig. 1, were analyzed for 60 s each, using a primary beam cross-section of 0.5 × 0.5 mm^2 and a secondary beam height of 0.03 mm. The diffraction angle was

Table 1 Chemical composition of X2CrNi18-9 (1.4307) in wt.%; other elements each < 0.04 wt.%

C	Si	Mn	Cr	Mo	Ni	Co	Cu	V	N	Fe
0.020	0.33	1.77	18.23	0.28	7.97	0.19	0.39	0.06	0.07	70.57

Table 2 Chemical composition of X6Cr17 (1.4016) in wt.%; other elements each < 0.02 wt.%.

C	Si	Mn	Cr	Mo	Ni	Co	Cu	V	N	Fe
0.065	0.48	0.41	16.42	0.03	0.11	0.02	0.05	0.10	0.05	82.23

Table 3 Mechanical properties of X2CrNi18-9 at room temperature in rolling (0°) and transverse (90°) directions

	Hot-rolled (as received)		After 1050 °C for 12 min	
Quantity/unit	**0°**	**90°**	**0°**	**90°**
σ_y/MPa	322 ± 2	322 ± 6	305 ± 8	302 ± 1
UTS/MPa	700 ± 5	708 ± 4	687 ± 1	680 ± 4
Fracture strain/%	75.6 ± 6.2	76.8 ± 3.5	75.3 ± 1.8	72.9 ± 1.5
E/MPa	193850			
Poisson ratio	0.282			

Table 4 Mechanical properties of X6Cr17 at room temperature in rolling (0°) and transverse (90°) directions.

	Hot-rolled (as received)		After 800 °C for 20 min	
Quantity/unit	**0°**	**90°**	**0°**	**90°**
σ_y/MPa	264 ± 1	292 ± 2	251 ± 2	274 ± 3
UTS/MPa	424 ± 2	474 ± 1	417 ± 2	463 ± 4
Fracture strain/%	40.4 ± 2.2	29.2 ± 0.6	31.3 ± 1.3	28.0 ± 1.7
E/MPa	209450	229300		
Poisson ratio	0.242	0.278		

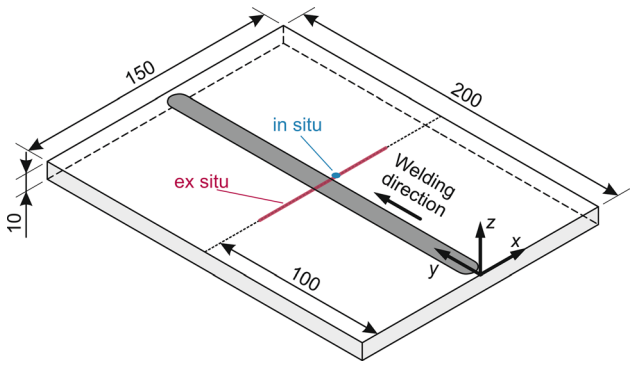

Fig. 1 Sample geometry, coordinate system and locations of in situ and ex situ analyses. Temperatures at the in situ measurement locations have been determined outside of the synchrotron

set at $2\theta = 16°$ and nine tilt angles of $\psi = 0°$, 18.43°, 26.57°, 33.21°, 39.23°, 45°, 50.77°, 56.79° and 63.43° were used, resulting in values of $\sin^2 \psi = 0 \ldots 0.8$. Here, the bar-shaped gauge volume was immersed into the specimen until half its height.

2.4 Analysis of Microstructure

The crystallite size D and microstrain e were determined by line profile analysis according to the method by Thompson, Cox & Hastings (Ref 17) adapted for energy-dispersive measurements (Ref 18). For the austenitic steel X2CrNi18-9, the reflections at the families of lattice planes {111}, {200}, {220} and {311} at $\psi = 0°$ were analyzed, whereas for the ferritic steel X6Cr17 {110}, {200}, {211} and {220} were used. Each diffractogram was corrected for detector dead time, the energy-dependent wiggler spectrum (Ref 16) and the storage ring current. The background intensity of the single peaks was subtracted using a linear fit function and the peaks were fitted by a pseudo-Voigt function. From the measured peak parameters, the instrumental parameters were subtracted, which have been determined with the LaB_6 standard reference material 660b by NIST (Ref 19). Only physically meaningful results with $0\ \text{nm} < D \leq 1000\ \text{nm}$ and $e \geq 10^{-4}$ were considered.

From the crystallite size and microstrain, the dislocation density ρ was determined according to Williamson and Smallman (Ref 20).

2.5 Stress Analysis

During welding, the in-plane stress $\sigma_{\parallel}$ was determined using the *transverse contraction method* (Ref 15). To this end, the same reflections were used as for the microstructure analysis, complemented by {222} or {310} for X2CrNi18-9 and X6Cr17, respectively. For each reflection at $\psi = 0°$, the normalized lattice distance $a^{hkl}_{\psi=0°}$ over time was determined and smoothed by a Savitzky-Golay filter before stress computation. The diffraction elastic constants (DEC) S_1^{hkl} at room

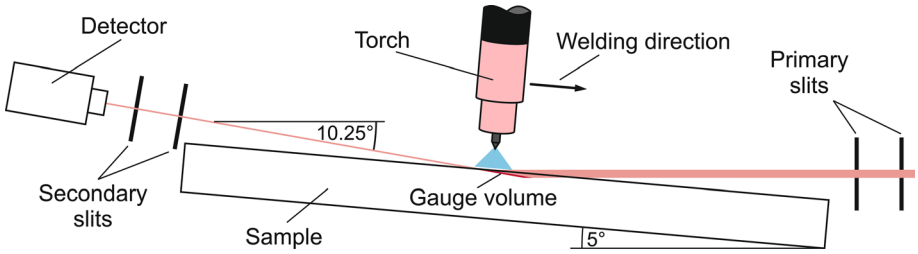

Fig. 2 Side view of in situ measurement setup (not drawn to scale)

temperature were computed from the single crystal elastic moduli of austenite and ferrite given in (Ref 21), see Table 5, initially using the model of Eshelby/Kröner (Ref 22, 23) and are listed in Tables 6 and 7. Since no DEC were available at higher temperatures, temperature-dependent literature values of the bulk elastic modulus were used to scale the DEC according to the time-dependent temperature at the point of measurement:

$$S_1^{hkl}(T) = S_1^{hkl}(T = 20°C) \cdot \frac{E(T = 20°C)}{E(T)} \qquad \text{(Eq 1)}$$

Here, $S_1{}^{hkl}(T = 20\ °C)$ are the DEC at room temperature as given in Tables 6, 7, 8 and 9, $E(T = 20\ °C)$ is the bulk elastic modulus at room temperature and $E(T)$ is the temperature-dependent bulk elastic modulus, where both $E(T = 20\ °C)$ and $E(T)$ are taken from (Ref 24, 25) for austenite and ferrite, respectively.

For the ex situ measurements, the residual stresses in both longitudinal and transverse directions of the weld, $\sigma_l{}^{RS}$ and $\sigma_t{}^{RS}$, were determined by the $\sin^2\psi$ method (Ref 26). To this end, the ten or eight reflections and the corresponding DEC $1/2S_2{}^{hkl}$ listed in Tables 6 and 7 for austenite and ferrite, respectively, were used to compute the mean stress value at each point of measurement. This was done by normalizing the measured lattice distance of each reflection {hkl} to the {100} plane, averaging them weighted by the number of equivalent planes {hkl} in a unit cell and converting the slope over $\sin^2\psi$ to the residual stress value through a weighted average DEC $1/2S_2{}^{av}$. This stress value is valid at an average penetration depth of 34 μm. Additionally, the in-plane residual stress $\sigma_{\parallel}{}^{RS} = 1/2(\sigma_l{}^{RS} + \sigma_t{}^{RS})$ resulting from the $\sin^2\psi$ method was compared to the results of the transverse contraction method for validation, using only the ex situ measurements at $\psi = 0°$ with the beam direction parallel ($\varphi = 0°$) or perpendicular ($\varphi = 90°$) to the welding direction.

3. Methodological Validation and Discussion

Figure 3 shows a comparison of the in-plane residual stresses derived from the transverse contraction and $\sin^2\psi$ methods for the ex situ measurements. Besides larger scatter, it can be seen that the transverse contraction method yields significantly higher stress values than the $\sin^2\psi$ method. Since the results of the former largely depend on the differences $\Delta(2S_1{}^{hkl})$, it can be inferred that the assumptions of the Eshelby/Kröner grain interaction model are not valid in this case.

Table 5 Single crystal elastic moduli of austenite (γ-Fe) and ferrite (α-Fe) in GPa, from (Ref 21)

Material	c_{11}	c_{12}	c_{44}
γ-Fe	233	163	122
α-Fe	230	135	114

In order to check this hypothesis, $S_1{}^{hkl}$ computed with the Eshelby/Kröner model is plotted against the orientation factor $3\Gamma = 3(h^2k^2 + k^2l^2 + l^2h^2)/(h^2 + k^2 + l^2)^2$ in comparison to $S_1{}^{\{311\}}$ and $S_1{}^{\{220\}}$ that have been determined experimentally for the austenitic steel X2CrNi18-9, see Fig. 4. It can be seen that the linear slope of the computed values is smaller than that of the measured and extrapolated ones by a factor of 0.64, meaning that also the differences $\Delta(2S_1{}^{hkl})$ are smaller by that factor. This corresponds to a Reuss ratio of $r_R = 0.57$ for the measured DEC, which yields a softer material behavior than according to the Eshelby/Kröner model, featuring $r_R = 0.365$, and thereby lower stresses.

In the following, both $S_1{}^{hkl}$ and $½S_2{}^{hkl}$ will be used with $r_R = 0.57$, see Tables 8 and 9. While this proposed correction is only based on two experimental values and the linear extrapolation shown in Fig. 4 thereby involves a high uncertainty, a comparison of the results of the transverse contraction and the $\sin^2\psi$ methods with corrected DEC $S_1{}^{hkl}$ and $½S_2{}^{hkl}$ shown in Fig. 5 proves that a much better agreement of the two methods is achieved.

For the ferritic steel X6Cr17, two experimentally determined values of $S_1{}^{hkl}$ were not available. Using the same correction with $r_R = 0.57$ as for X2CrNi18-9 yields a very good agreement of the transverse contraction and the $\sin^2\psi$ methods as well, see Fig. 6. Therefore, the same correction will be used for X6Cr17 in the following.

The results shown above mean that the Eshelby/Kröner model assumes DEC that are too stiff at the surface, which has also been found by other authors (Ref 27). It should be noted that the DEC optimization scheme introduced in (Ref 15, 28), which is based on the energy dependence of the penetration depth and which was run at x = − 10 mm for X2CrNi18-0 and at $x = 9$ mm for X6Cr17, yielded optimum values of $r_R = 0.535$ and $r_R = 0.560$, respectively. This confirms the value of $r_R = 0.57$ and thereby the approach taken. Potentially, a direct comparison of the results of the transverse contraction and the $\sin^2\psi$ methods through a systematic variation of the Reuss ratio could also be used for an optimization of the DEC.

Table 6 DEC of austenite (γ-Fe) according to the Eshelby/Kröner model in 10^{-6} mm²/N; for double peak weighted according to number of equivalent planes in unit cell

DEC	{111}	{200}	{220}	{311}	{222}	{400}	{331}	{420}	{422}	{333}{511}
S_1^{hkl}	− 1.11	− 2.35	− 1.43	− 1.77	− 1.11	− 2.35	− 1.34	− 1.76	− 1.43	− 1.85
$1/2S_2^{hkl}$	5.14	8.86	6.07	7.11	5.14	8.86	5.79	7.07	6.07	7.34

Table 7 DEC of ferrite (α-Fe) according to the Eshelby/Kröner model in 10^{-6} mm²/N; for double peak weighted according to number of equivalent planes in unit cell

DEC	{110}	{200}	{211}	{220}	{310}	{222}	{321}	{330}{411}
S_1^{hkl}	− 1.27	− 1.90	− 1.27	− 1.27	− 1.67	− 1.05	− 1.27	− 1.51
$1/2S_2^{hkl}$	5.80	7.70	5.80	5.80	7.02	5.17	5.80	6.55

Table 8 Corrected DEC of austenite (γ-Fe) in 10^{-6} mm²/N, using a Reuss ratio of $r_R = 0.57$; for double peak weighted according to number of equivalent planes in unit cell

DEC	{111}	{200}	{220}	{311}	{222}	{400}	{331}	{420}	{422}	{333}{511}
S_1^{hkl}	− 1.00	− 2.94	− 1.49	− 2.03	− 1.00	− 2.94	− 1.35	− 2.01	− 1.49	− 2.15
$1/2S_2^{hkl}$	4.80	10.6	6.26	7.88	4.80	10.6	5.83	7.82	6.26	8.24

Table 9 Corrected DEC of ferrite (α-Fe) in 10^{-6} mm²/N, using a Reuss ratio of $r_R = 0.57$; for double peak weighted according to number of equivalent planes in unit cell

DEC	{110}	{200}	{211}	{220}	{310}	{222}	{321}	{330}{411}
S_1^{hkl}	− 1.28	− 2.20	− 1.28	− 1.28	− 1.87	− 0.969	− 1.28	− 1.64
$1/2S_2^{hkl}$	5.84	8.61	5.84	5.84	7.62	4.92	5.84	6.93

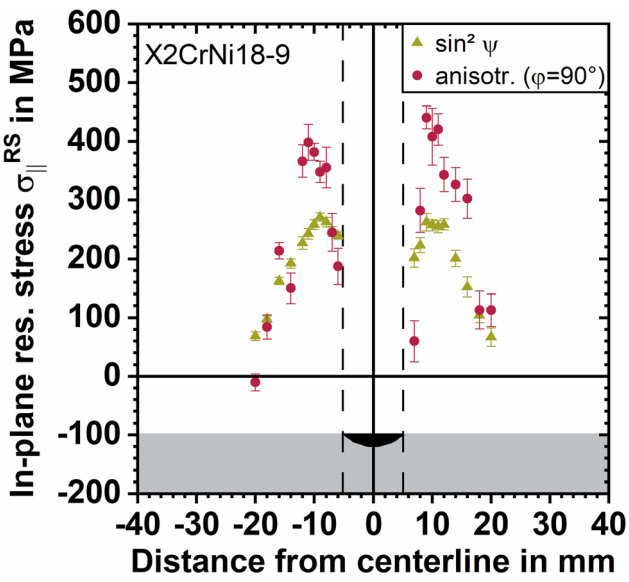

Fig. 3 Comparison of the in-plane residual stresses derived from transverse contraction and $\sin^2\psi$ method for X2CrNi-18-9

4. Results

4.1 Microscopy

In Fig. 7 and 8, light optical microscope images of a cross-section of the weld zone of X2CrNi18-9 and X6Cr17 are depicted, respectively, after sample preparation with V2A etchant. The molten zones show elongated, radially arranged grains and a relatively low depth of 1.5 … 2 mm. For X2CrNi18-9, the base material in the near vicinity features the same microstructure as in the non-welded state, whereas for X6Cr17 a HAZ of about 1 mm width is clearly visible, see Fig. 8(b). It features coarse, equiaxed grains which get finer with increasing distance from the molten zone. Both in the HAZ and the molten zone, martensite occurs especially near the grain boundaries, hinting at a partial phase transformation of X6Cr17 due to the thermal cycle.

4.2 Evolution of Stress and Microstructure during Welding

Figure 9 shows an exemplary stress analysis of the in-situ measurements using the transverse contraction method for X2CrNi18-9 at a distance of $x = 7$ mm. In Fig. 9(a), the

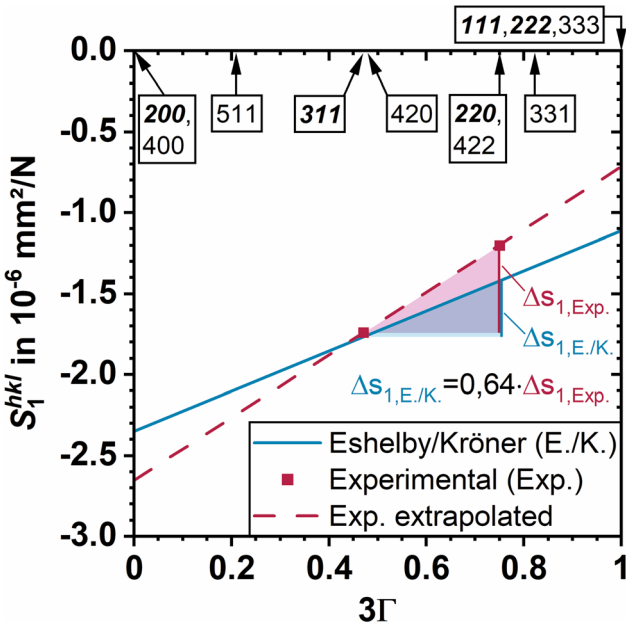

Fig. 4 S_1^{hkl} versus orientation factor 3Γ computed with Eshelby/Kröner model and measured experimentally; diffraction peaks ***hkl*** used in the in situ analyses are printed in bold/italic font

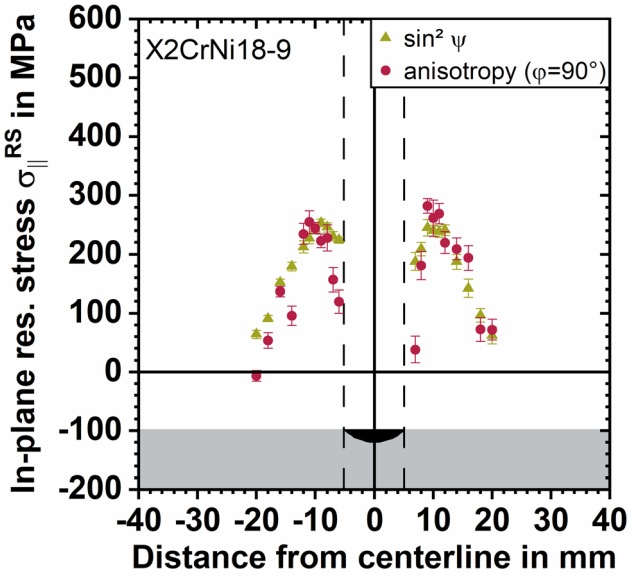

Fig. 5 Comparison of the in-plane residual stresses derived from transverse contraction and $\sin^2\psi$ method after correction of $\Delta(2S_1^{hkl})$ for X2CrNi18-9

normalized lattice distance $a_{\psi=0°}^{hkl}$ over time for is depicted for reflections on different lattice planes {hkl}, clearly highlighting the thermal strains due to heating. Figure 9(b)-(e) shows the relative strains ε_r between these differently oriented grains over the differences in the diffraction elastic constants $\Delta(2S_1^{hkl})$ evaluated at different points of time. Here, the data points were fitted with a linear function whose slope is the average in-plane stress $\sigma_{||}$. A positive slope indicates tensile stress, whereas a negative one indicates compressive stress.

In the following diagrams, the results of the in situ measurements are presented over a logarithmic time scale in order to cover both short-term effects during welding and the near-final state toward the end of the cooling period. The plots show the evolutions of the in-plane stress $\sigma_{||}$, the square-root of the dislocation density $\rho^{1/2}$ and the temperature T over time t. One plot pertains to a single point of measurement on a single sample. For $\sigma_{||}$, only every fifth data point is shown for $t > 100$ s for better visualization. Also, the error bars of $\rho^{1/2}$ are only shown exemplarily for a few data points; the ones not shown are of the same order of magnitude.

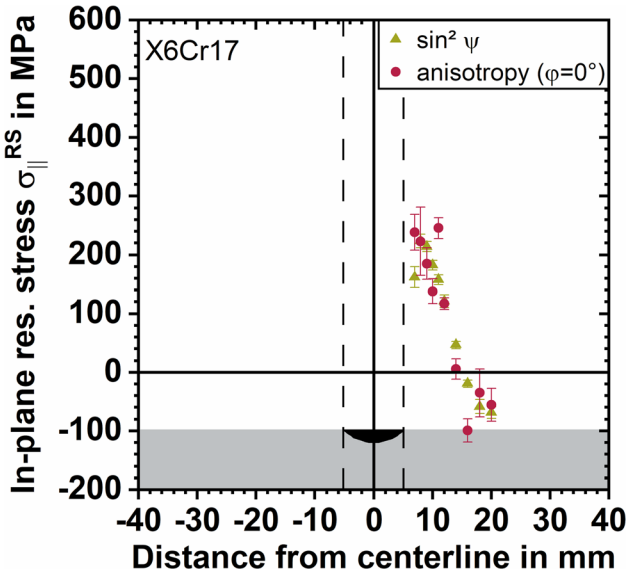

Fig. 6 Comparison of the in-plane residual stresses derived from transverse contraction and $\sin^2\psi$ method after correction of $\Delta(2S_1^{hkl})$ for X6Cr17

For X2CrNi18-9 at $x = 7$ mm, compressive stress develops rapidly during heating and reaches a maximum absolute value of about − 300 MPa shortly before the maximum temperature occurs, see Fig. 10. Within a few seconds, the sign of the stress changes and a relative maximum of 170 MPa is reached during cooling. After a relative minimum that coincides with the end of the welding process, the stress asymptotically approaches a value of 200 MPa.

The square-root of the dislocation density $\rho^{1/2}$ is 1.0 … 1.4 · 10^7 m^{-1} at the beginning of the welding process. After the maximum temperature is reached, $\rho^{1/2}$ increases to about 1.7 · 10^7 m^{-1}, but a large scatter can be observed. The scatter decreases for $t > 300$ s due to the longer integration times of the diffraction peaks and $\rho^{1/2}$ remains constant within 1.8 … 2.0 · 10^7 m^{-1} toward the end of the cooling process. It may be noted that the error bars derived from the uncertainties of the peak fit comprise a span much larger than the range of the actually measured values.

At $x = 9$ mm, the $\sigma_{||}$-t-curve is similar to the one at $x = 7$ mm, but exhibits no distinct tensile maximum after reaching T_{max}, see Fig. 11. The same value of 200 MPa is taken at the end of the cooling process. $\rho^{1/2}$ starts at about 1.7 · 10^7 m^{-1}, shows a distinct maximum of 2.9 · 10^7 m^{-1} during heating and finishes in the same range as at $x = 7$ mm. However, a larger scatter of $\rho^{1/2}$ is generally observed here.

For X6Cr17 at $x = 7$ mm, the evolution of $\sigma_{||}$ is qualitatively the same as for X2CrNi18-9, see Fig. 12. However, there is significant compressive stress already at the beginning of the welding process. The absolute values of the minimum and

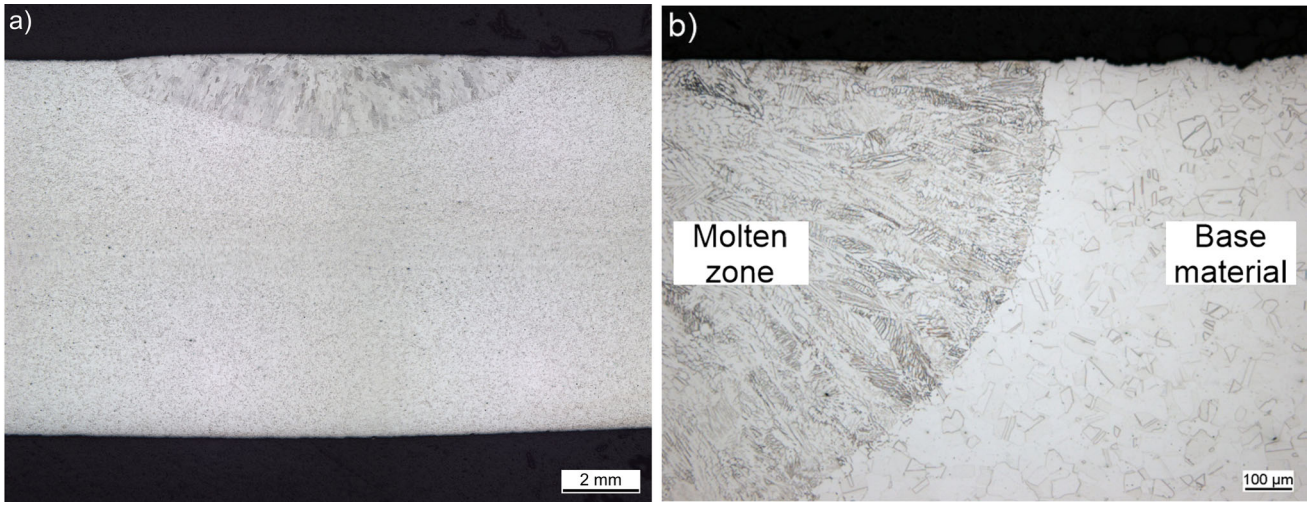

Fig. 7 Weld zone of X2CrNi18-9: (a) Macrograph; (b) Micrograph of molten zone and base material at lateral transition zone

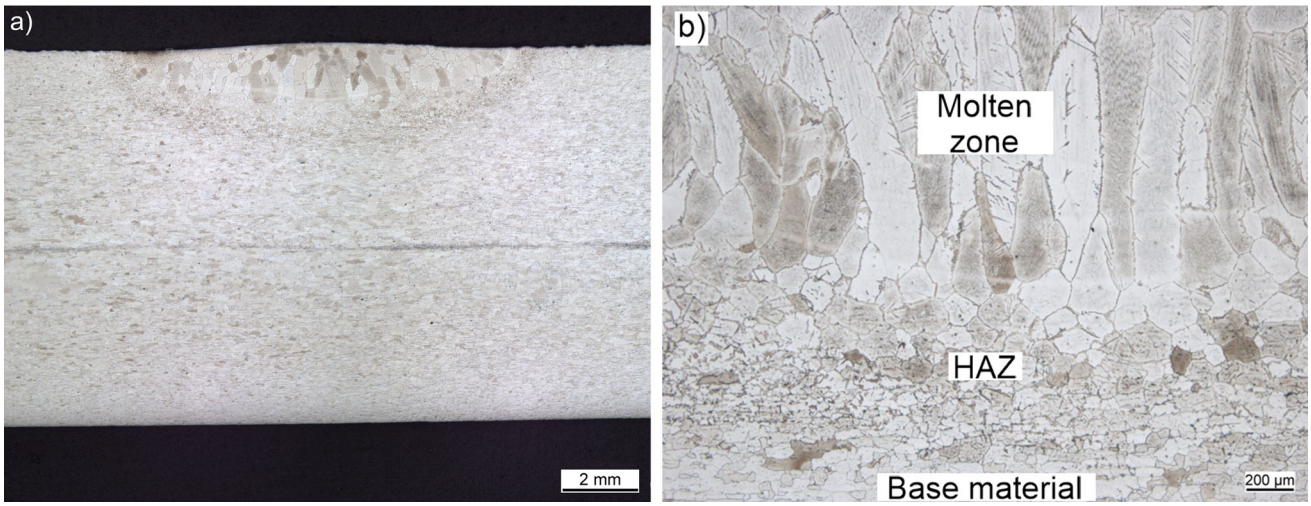

Fig. 8 Weld zone of X6Cr17: (a) Macrograph; (b) Micrograph of molten zone, heat-affected zone (HAZ) and base material at lower transition zone

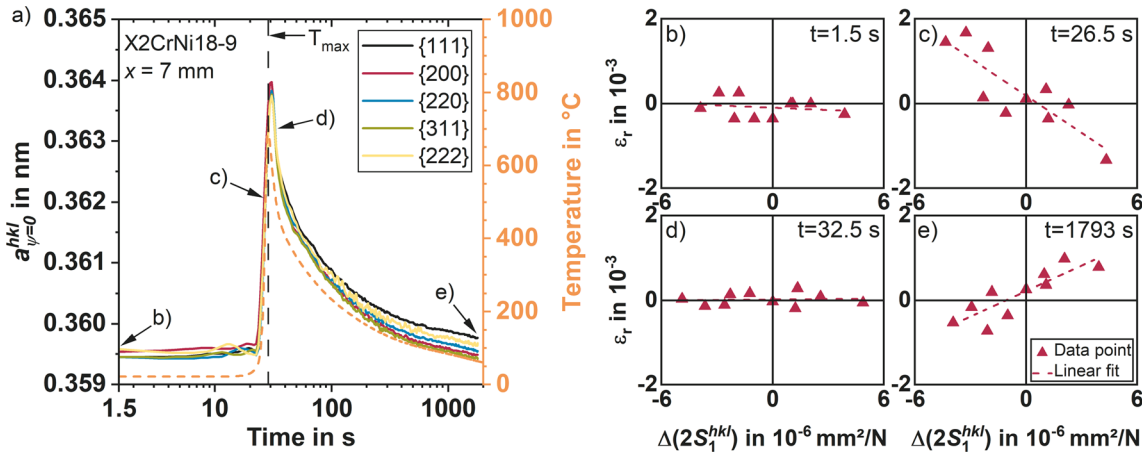

Fig. 9 Exemplary in-situ analysis using the transverse contraction method for X2CrNi18-9 at a distance of x = 7 mm: (a) Normalized lattice distance $a^{hkl}_{\psi=0°}$ over time for reflections on different lattice planes {hkl}; (b)-(e) Relative strains ε_r over the differences in the diffraction elastic constants $\Delta(2S_1{}^{hkl})$ evaluated at different points of time, see (a)

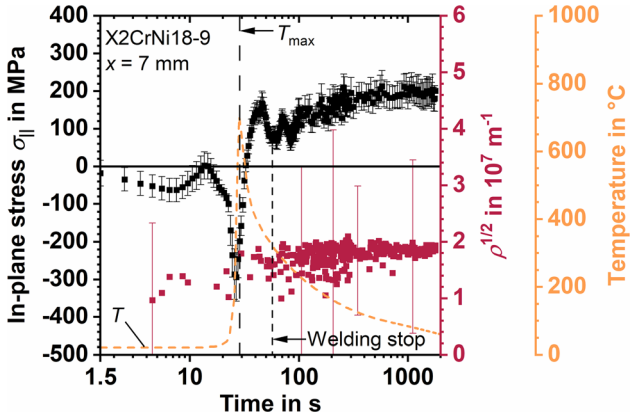

Fig. 10 Evolution of in-plane stress, square-root of dislocation density and temperature during welding and cooling of X2CrNi18-9 at a distance of $x = 7$ mm from the weld centerline. See text for details

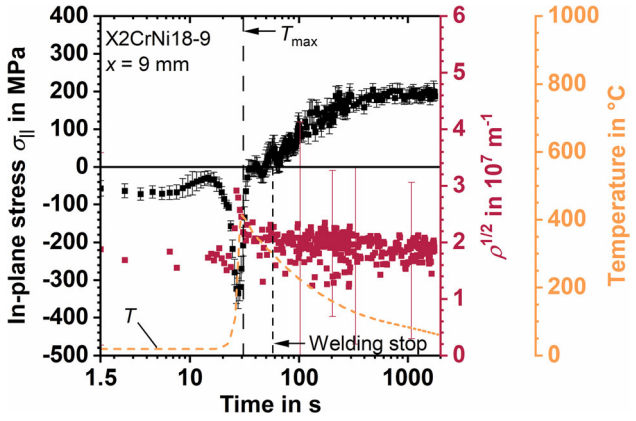

Fig. 11 Evolution of in-plane stress, square-root of dislocation density and temperature during welding and cooling of X2CrNi18-9 at a distance of $x = 9$ mm from the weld centerline. See text for details

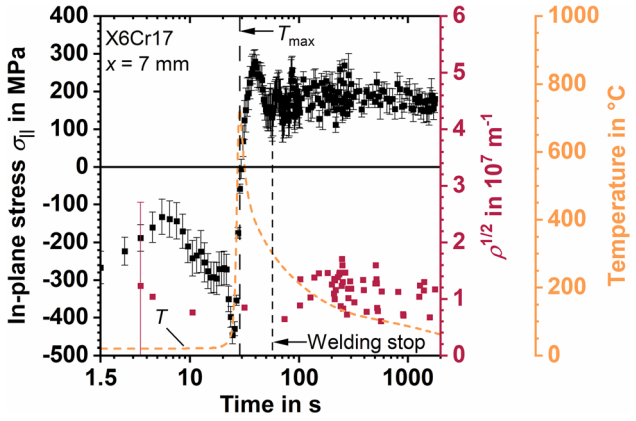

Fig. 12 Evolution of in-plane stress, square-root of dislocation density and temperature during welding and cooling of X7Cr17 at a distance of x = 7 mm from the weld centerline. See text for details

maximum stresses close to the temperature maximum are larger than for X2CrNi18-9, reaching − 450 and 280 MPa, respectively. The final value of $\sigma_{||}$ is about 170 MPa. The scatter of the data points is significantly larger than for X2CrNi18-9.

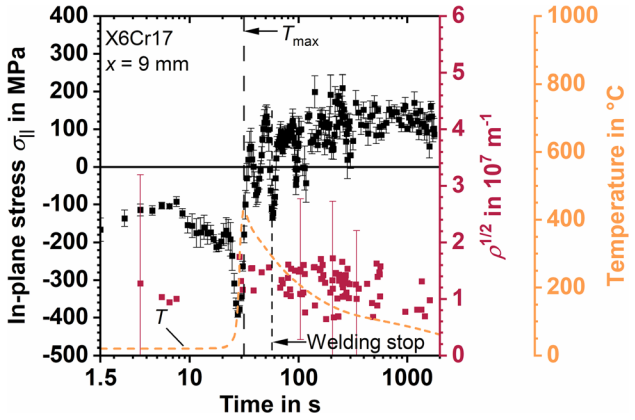

Fig. 13 Evolution of in-plane stress, square-root of dislocation density and temperature during welding and cooling of X6Cr17 at a distance of $x = 9$ mm from the weld centerline. See text for details

For $\rho^{1/2}$, only few significantly scattered data points exist both at x = 7 mm and at x = 9 mm, as can be seen in Fig. 13, permitting no further analysis of the dislocation density.

The in-plane stress at $x = 9$ mm, however, is qualitatively similar to that at the same point for X2CrNi18-9, but again accompanied by a larger scatter.

4.3 Residual Stress State

The residual stress distributions after complete cooling are M-shaped for both materials with distinct maxima close to the weld toe at $|x| \approx 8$ mm, see Fig. 14 and 15. The maximum longitudinal residual stresses are 400 … 430 MPa for X2CrNi18-9 and 370 MPa for X6Cr17, whereas the transverse residual stresses only reach 140 or 75 MPa, respectively. Within the molten zone, no results could be achieved due to the large grains. The von Mises equivalent residual stress largely follows the longitudinal one and surpasses the materials' initial yield stresses.

It should be noted that the average of longitudinal and transverse residual stresses determined by the $\sin^2\psi$ method yields the in-plane residual stresses plotted in Fig. 5 and 6.

5. Discussion

5.1 Quality of Results

A comparison of the results of the in situ stress analysis in Fig. 10, 11, 12 and 13 reveals that the scatter is significantly larger for the ferritic steel X6Cr17 than for the austenitic steel X2CrNi18-9. This is due to the use of the transverse contraction method, whose results depend directly on the DEC differences $\Delta(2S_1^{hkl})$, in combination with two characteristics of the body-centered cubic (bcc) ferritic steel. Firstly, the crystal anisotropy is lower for bcc than for face-centered cubic (fcc) austenite, which can be seen in the smaller differences $\Delta(2S_1^{hkl})$, see Tables 8 and 9, or in the lower Zener anisotropy ratio $A = 2c_{44}/(c_{11}-c_{12})$ (Ref 29), which is 2.4 for ferrite and 3.5 for austenite, using the single crystal constants given in Table 5. Secondly, the orientation factors of the five lattice planes used in the in situ analyses for ferrite only cover the span $3\Gamma = 0 \ldots 0.75$,

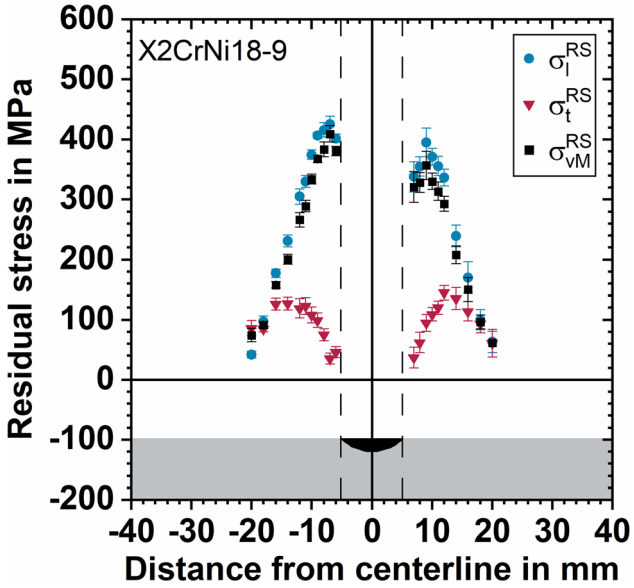

Fig. 14 Longitudinal (σ_l^{RS}), transverse (σ_t^{RS}) and von Mises equivalent (σ_{vM}^{RS}) residual stresses for X2CrNi18-9

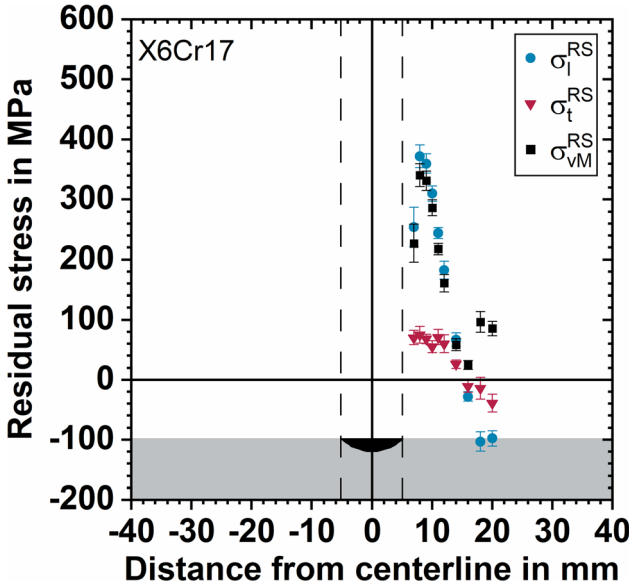

Fig. 15 Longitudinal (σ_l^{RS}), transverse (σ_t^{RS}) and von Mises equivalent (σ_{vM}^{RS}) residual stresses for X6Cr17

whereas for austenite the full scale $3\Gamma = 0 \ldots 1$ is used. This means that the total span of $\Delta(2S_1^{hkl})$ is smaller, making a linear fit of the relative strains between differently oriented grains over $\Delta(2S_1^{hkl})$ less reliable (please refer to (Ref 15) for a detailed description of the method). Moreover, the three diffraction peaks yielding the highest intensity and therefore the most reliable information on the lattice distance, i.e., {110}, {211} and {220}, feature the same 3Γ and DEC, thereby contributing the same information to the analysis. The other two diffraction peaks {200} and {310} are the weakest ones and therefore have the highest uncertainties with regard to the lattice distance. A higher total scatter of $\sigma_{||}$ results from these circumstances for X6Cr17, especially for short integration times during measurement.

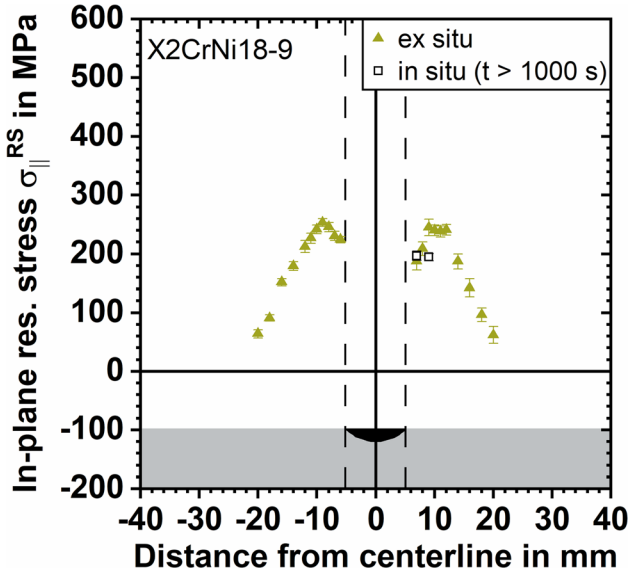

Fig. 16 Comparison of the in-plane residual stress $\sigma_{||}^{RS}$ at the end of the in situ analyses (transverse contraction method, averaged for $t > 1000$ s) and the ex situ analysis ($\sin^2\psi$ method) for X2CrNi18-9

The analysis of the square root of the dislocation density $\rho^{1/2}$ is subject to a higher scatter than the stress analysis since the latter relies on the position of the diffraction peaks, which is easier to determine than the shape of the diffraction peaks needed for the former. This is especially true for short integration times, as can be seen, e.g., in the lower scatter in Fig. 10 toward the end of the cooling process. Moreover, a rapid change of the lattice strain due to thermal expansion and/or high stress rates may lead to an apparent peak broadening due to smearing over the integration time. This could be an explanation for the seemingly high dislocation density when the maximum temperature is reached, see Fig. 11.

Despite these challenges, the results of $\rho^{1/2}$ permit some conclusions for X2CrNi18-9, see section 5.3 (Effects of the Welding Process on Stress and Work Hardening Near the Molten Zone).

5.2 Consistency of Results

In the final stage of cooling, the in-plane stress $\sigma_{||}$ reaches a steady state value which can be compared to the ex situ results to check the consistency of the measurements. To this end, the in situ results are averaged for $t > 1000$ s and plotted against the respective measurement position along with the ex situ results, see Fig. 16 and 17. Since for $t > 1000$ s the temperatures are still in the range $T = 86 \ldots 61$ °C, the elastic behavior of the material is slightly softer than after complete cooling. However, the error can be estimated to be less than 2%, so that a comparison of the results obtained in situ and ex situ is permissible.

Overall, a very good agreement of in situ and ex situ results is observed. Only for X6Cr17 at $x = 9$ mm, a deviation of about 100 MPa is noted. Apart from regular measurement uncertainties, deviations are mainly attributed to the different gauge volumes, which were larger and fully immersed for the in situ measurements, whereas they were smaller and only partially immersed into the material for the ex situ measurements. Moreover, due to the elongate, bar-shaped geometry of the gauge volume and the high lateral stress gradients in the

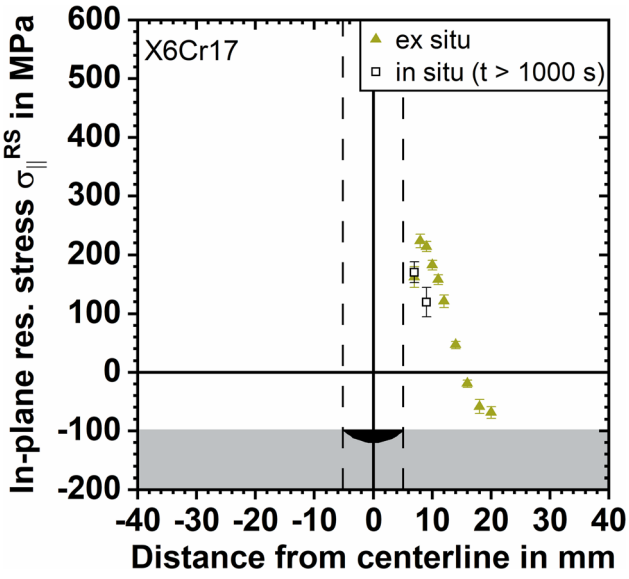

Fig. 17 Comparison of the in-plane residual stress $\sigma_{\parallel}^{RS}$ at the end of the in situ analyses (transverse contraction method, averaged for $t > 1000$ s) and the ex situ analysis ($\sin^2\psi$ method) for X6Cr17

vicinity of the weld, the angle of the beam to the welding direction as well as the tilt angle ψ of the sample can significantly affect the results.

5.3 Effects of the Welding Process on Stress and Work Hardening Near the Molten Zone

The results of the in situ measurements depicted in Fig. 10, 11, 12 and 13 clearly highlight the compression-tension cycle near the molten zone for both materials. The mechanical stresses thereby reflect the constrained thermal expansion and contraction during welding and cooling. The fact that the maximum compressive stresses always occur before the maximum temperature is reached shows that a zone of compressive stresses runs ahead of the heat source since the highly heated material expands and thereby compresses the base material, which is also described, e.g., in (Ref 1).

For the austenitic steel X2CrNi18-9, the high stresses cause work hardening of the material, which can be seen in a slight, but clearly identifiable increase of the square-root of the dislocation density $\rho^{1/2}$ directly after the maximum compressive stress has occurred. Afterward, only small changes of the dislocation density can be seen. Firstly, this reveals that the main plastic deformation results from the compressive stress during heating, which has a higher absolute value than the tensile stress during cooling. Secondly, these results give no direct indication on the nature of work hardening, i.e., its isotropic or kinematic character, as the evolution of $\rho^{1/2}$ in the tensile phase is not clear due to the small changes of time and the relatively large scatter.

However, the ex situ results have shown that the von Mises equivalent residual stresses are M-shaped and surpass the materials' initial yield strengths a few millimeters away from the weld. This proves that plastic deformation has occurred and confirms previous analyses hinting at isotropic hardening behavior (Ref 11).

For the ferritic steel X6Cr17, the observed scatter of $\rho^{1/2}$ does not permit similar conclusions as for X2CrNi18-9. Since the material shows a similar material behavior, including M-shaped residual stresses with high maxima, it is inferred that isotropic hardening predominates here as well, which has to be confirmed by further analyses.

6. Summary and Conclusions

A novel method of stress analysis exploiting crystallite anisotropy was employed to study the stress evolution in situ during welding with energy-dispersive x-ray diffraction. The results obtained with this method were validated with a $\sin^2\psi$ analysis. Moreover, line profile analysis was used to gain information on the microstructure and thereby the hardening behavior of the materials. The following conclusions can be drawn:

1. With the transverse contraction method introduced in (Ref 15), stresses can be determined reliably in practice. The method is especially valuable for situations where tilting the sample is not possible, e.g., for fast in situ analyses or for complex sample geometries for which tilting may result in beam shadowing. The information obtained through the transverse contraction method is limited though, e.g., only yielding the average in-plane stress for measuring at $\psi = 0°$. Potentially, this could be remedied by a multi-detector setup measuring at different tilt angles, if possible.
2. The results of the transverse contraction method depend significantly on the applied DEC. Therefore, care must be taken when a grain interaction model is chosen. Preferably, the correct DEC should be found by an optimization scheme. This can be done either by varying the DEC and iteratively comparing the results of the transverse contraction and the $\sin^2\psi$ methods for a sample with significant stresses that are constant over depth. Or the optimization scheme that is also introduced in (Ref 15, 28) is used, which exploits the energy dependence of the penetration depth of the "white" X-ray beam.
3. The transverse contraction method yielded better results for the austenitic steel than for the ferritic one. This highlights that the method works best for high anisotropy ratios A and for reflections hkl with significantly different orientation factors 3Γ.
4. The in situ stress analysis revealed the compression-tension cycle in the vicinity of the weld. The stresses in the final stages of cooling mostly agree with the residual stresses determined through ex situ analyses, again emphasizing the suitability of the transverse contraction method.
5. The line profile analysis yielded the dislocation density, which was subject to relatively large scatter due to the short measurement intervals during welding. However, it proved that significant plastic deformation occurs in X2CrNi18-9 due to the compressive stresses during heating.
6. The ex situ analyses hint toward a mostly isotropic hardening behavior near the molten zone, but more analyses are necessary to confirm this conclusion.

Acknowledgments

The authors gratefully acknowledge the financial support of the Deutsche Forschungsgemeinschaft (DFG) through research project number 273371116. We thank the Helmholtz-Zentrum Berlin für Materialien und Energie for the allocation of synchrotron radiation beamtime.

Funding

Open Access funding enabled and organized by Projekt DEAL.

Open Access

This article is licensed under a Creative Commons Attribution 4.0 International License, which permits use, sharing, adaptation, distribution and reproduction in any medium or format, as long as you give appropriate credit to the original author(s) and the source, provide a link to the Creative Commons licence, and indicate if changes were made. The images or other third party material in this article are included in the article's Creative Commons licence, unless indicated otherwise in a credit line to the material. If material is not included in the article's Creative Commons licence and your intended use is not permitted by statutory regulation or exceeds the permitted use, you will need to obtain permission directly from the copyright holder. To view a copy of this licence, visit http://creativecommons.org/licenses/by/4.0/.

References

1. D. Radaj, *Heat Effects of Welding: Temperature Field, Residual Stress, Distortion*, Springer, Berlin, 1992
2. A.S. Khan and S. Huang, *Continuum Theory of Plasticity*, Wiley, New York, 1995
3. J.L. Chaboche, Viscoplastic Constitutive Equations for the Description of Cyclic and Anisotropic Behaviour of Metals, *B. Acad. Pol. Sci. Tech.*, 1977, **25**(1), p 33–42.
4. T. Loose, J. Sakkiettibutra, and H. Wohlfahrt, New 3D-calculations of residual stresses consistent with measured results of the IIW Round Robin programme, Mathematical modelling of weld phenomena 9, *International Seminar "Numerical Analysis of Weldability."* H.-H. Cerjak, N. Enzinger Ed., Verlag der Technischen Universität Graz, Graz, 2010, p 369–390
5. H. Wohlfahrt, T. Nitschke-Pagel, K. Dilger, D. Siegele, M. Brand, J. Sakkiettibutra, and T. Loose, Residual Stress Calculations and Measurements—Review and Assessment of the IIW Round Robin Results, *Weld. World*, 2012 https://doi.org/10.1007/BF03321387
6. M.C. Smith, A.C. Smith, R. Wimpory, and C. Ohms, A Review of the NeT Task Group 1 Residual Stress Measurement and Analysis Round Robin on a Single Weld Bead-on-Plate Specimen, *Int. J. Pres. Ves. Pip.*, 2014 https://doi.org/10.1016/j.ijpvp.2014.05.002
7. M.C. Smith, O. Muránsky, C. Austin, P. Bendeich, and Q. Xiong, Optimised Modelling of AISI 316L(N) Material Behaviour in the NeT TG4 International Weld Simulation and Measurement Benchmark, *Int. J. Pres. Ves. Pip.*, 2018 https://doi.org/10.1016/j.ijpvp.2017.11.004
8. D. Deng, C. Zhang, X. Pu, and W. Liang, Influence of Material Model on Prediction Accuracy of Welding Residual Stress in an Austenitic Stainless Steel Multi-pass Butt-Welded Joint, *J. Mater. Eng. Perform.*, 2017 https://doi.org/10.1007/s11665-017-2626-6
9. M.J. Ottersböck, M. Stoschka, and M. Thaler, Study of kinematic strain hardening law in transient welding simulation, mathematical modelling of weld phenomena 10, *International Seminar "Numerical Analysis of Weldability."* C. Sommitsch, N. Enzinger Ed., Verlag der Technischen Universität Graz, Graz, 2013, p 255–266
10. N. Häberle, A. Pittner, R. Falkenberg, O. Kahlcke, and M. Rethmeier, Application of Multi-Phase Viscoplastic Material Modelling to Computational Welding Mechanics of Grade-S960QL steel, *CR Mécanique*, 2018 https://doi.org/10.1016/j.crme.2018.08.001
11. N. Hempel, T. Nitschke-Pagel, J. Rebelo Kornmeier, and K. Dilger, Experimental and Computational Analysis of Residual Stress and Mechanical Hardening in Welded High-Alloy Steels, Residual Stresses 2018, 1st edn, M. Seefeldt, Ed., Nov 9, 2018, Materials Research Forum LLC, 2018, p 227–232. https://doi.org/10.21741/9781945291890-36
12. C. Genzel, C. Stock, and W. Reimers, Application of Energy-Dispersive Diffraction to the Analysis of Multiaxial Residual Stress Fields in the Intermediate Zone Between Surface and Volume, *Mater. Sci. Eng. A-Struct.*, 2004 https://doi.org/10.1016/j.msea.2003.09.073
13. A. Kromm, T. Kannengiesser, and J. Gibmeier, In Situ Observation of Phase Transformations during Welding of Low Transformation Temperature Filler Material, *Mater. Sci. Forum*, 2010 https://doi.org/10.4028/www.scientific.net/MSF.638-642.3769
14. F. Niessen, D. Apel, F. Danoix, J. Hald, and M. Somers, Evolution of Substructure in Low-Interstitial Martensitic Stainless Steel During Tempering, *Mater Charact*, 2020 https://doi.org/10.1016/j.matchar.2020.110494
15. C. Genzel, M. Klaus, N. Hempel, T. Nitschke-Pagel, and K. Pantleon, Energy-Dispersive X-ray Stress Analysis under Geometric Constraints: Exploiting the Material's Inherent Anisotropy, *J. Appl. Crystallogr.*, 2023 https://doi.org/10.1107/S1600576723001759
16. M. Klaus and F. Garcia-Moreno, The 7T-MPW-EDDI Beamline at BESSY II, *JLSRF*, 2016 https://doi.org/10.17815/jlsrf-2-63
17. P. Thompson, D.E. Cox, and J.B. Hastings, Rietveld Refinement of Debye-Scherrer Synchrotron X-ray Data from Al_2O_3, *J. Appl. Crystallogr.*, 1987 https://doi.org/10.1107/S0021889887087090
18. D. Apel, M. Klaus, C. Genzel, and D. Balzar, Rietveld Refinement of Energy-Dispersive Synchrotron Measurements, *Z. Kristallogr.*, 2011 https://doi.org/10.1524/zkri.2011.1436
19. D.R. Black, D.A. Windover, A. Henins, J.J. Filliben, and J.P. Cline, Certification of Standard Reference Material 660b. https://www.nist.gov/publications/certification-standard-reference-material-660b. Accessed 16 June 2023
20. G.K. Williamson and R.E. Smallman III., Dislocation Densities in Some Annealed and Cold-Worked Metals from Measurements on the X-ray Debye-Scherrer Spectrum, *Phil. Mag.*, 1956 https://doi.org/10.1080/14786435608238074
21. M.M. Choy, K.-H. Hellwege, H. Landolt, R. Börnstein, and O. Madelung Eds., *Landolt-Börnstein Numerical Data and Functional Relationships in Science and Technology, Group III: Elastic, Piezoelectric, Pyroelectric, Piezooptic, Electrooptic Constants and Nonlinear Dielectric Susceptibilities of Crystals*, Springer, Berlin, 1979
22. J.D. Eshelby, The Determination of the Elastic Field of An Ellipsoidal Inclusion, and Related Problems, *Proc. R. Soc. Lond. A*, 1957 https://doi.org/10.1098/rspa.1957.0133
23. E. Kröner, Berechnung der elastischen Konstanten des Vielkristalls aus den Konstanten des Einkristalls, *Z. Phys.*, 1958 https://doi.org/10.1007/BF01337948,inGerman
24. O. Voß, Untersuchung relevanter Einflußgrößen auf die numerische Schweißsimulation, Ph.D. Thesis, Techn. Univ. Braunschweig, Shaker, Aachen, 2001 (in German)
25. T. Manninen and Säynäjäkangas J., mechanical properties of ferritic stainless steels at elevated temperature, in *Stainless Steel in Structures - Fourth International Experts Seminar*, http://www.steel-stainless.org/media/1124/32_manninen_t.pdf. Accessed 16 June 2023 (2012)
26. E. Macherauch and P. Müller, Das $\sin^2 \psi$-Verfahren der röntgenographischen Spannungsmessung, *Z. Angew. Phys.*, 1961, **13**, p 305–312. (**in German**)
27. A. Baczmanski, A. Tidu, P. Lipiński, M. Humbert, and K. Wierzbanowski, New Type of Diffraction Elastic Constants for Stress Determination, *Mater. Sci. Forum*, 2006 https://doi.org/10.4028/www.scientific.net/MSF.524-525.235
28. M. Klaus and C. Genzel, Reassessment of Evaluation Methods for the Analysis of Near-Surface Residual Stress Fields Using Energy-Dispersive Diffraction, *J. Appl. Crystallogr.*, 2019 https://doi.org/10.1107/S1600576718018095
29. C. Zener, *Elasticity and Anelasticity of Metals*, University of Chicago Press, Berlin, 1948

Publisher's Note Springer Nature remains neutral with regard to jurisdictional claims in published maps and institutional affiliations.